JOURNAL OF THERMOPHYSICS AND HEAT TRANSFER
Vol. 21, No. 4, October–December 2007

Boundary Layers on a Flat Plate at Sub- and Superorbital Speeds

Michael J. Hayne* and David J. Mee†
The University of Queensland, Brisbane, Queensland 4072, Australia
Sudhir L. Gai‡
University of New South Wales, Australian Defence Force Academy, Canberra, Australian Capital Territory 2600, Australia
and
Timothy J. McIntyre§
The University of Queensland, Brisbane, Queensland 4072, Australia

DOI: 10.2514/1.26894

The heat flux and boundary layers over a flat plate at suborbital and superorbital speeds were measured in a free-piston expansion tube at enthalpies of 26.0 and 53.4 MJ/kg, respectively. Estimates of the gas-phase and surface Damköhler numbers were made that indicate that although the boundary layer might be frozen, there is a possibility of surface reactions occurring. The heat-flux results were compared with theoretical predictions of heat flux for both frozen and equilibrium chemistries. The results indicated that the influence of real gas effects, such as recombination and surface catalycity, were minimal for the present flow conditions. Interferograms were obtained using resonance enhancement of the thermal boundary layer over a flat plate. Comparison of the measured boundary-layer thickness with several expressions used to predict the boundary-layer thickness allowed an evaluation of their effectiveness at high enthalpies.

Nomenclature

C	=	Chapman–Rubesin parameter
C_f	=	local skin friction coefficient
C_i	=	mass fraction of species i
C_w	=	ratio of density–viscosity product evaluated at the wall and edge of the boundary layer
c_p	=	specific heat at constant pressure
dt	=	time step
F	=	empirical correction factor
h	=	enthalpy
h^0	=	enthalpy of formation
k	=	reaction rate
k_R	=	specific recombination rate coefficient
M	=	Mach number
Pe	=	Peclet number
Pr	=	Prandtl number
q	=	heat flux
Re_x	=	Reynolds number
R_G	=	gauge resistance
R_0	=	universal gas constant
Sc	=	Schmidt number of gas mixture
St	=	Stanton number
T	=	temperature
u	=	velocity
x	=	streamwise distance
γ	=	ratio of specific heats
δ	=	boundary-layer thickness
ρ	=	density
τ	=	characteristic time
ω	=	exponent of temperature
Ω_g	=	gas-phase Damköhler number
Ω_s	=	surface Damköhler number

Subscripts

chem	=	chemical component
d	=	diffusion
e	=	edge of the boundary layer
eq	=	equilibrium conditions
f	=	frozen conditions
r	=	recovery value, reaction (time)
s	=	surface
vib	=	vibrational component
w	=	wall value
0	=	stagnation

Superscripts

*	=	reference value

Received 2 August 2006; revision received 9 March 2007; accepted for publication 10 March 2007.

*Postgraduate Student, Division of Mechanical Engineering, School of Engineering.
†Associate Professor, Division of Mechanical Engineering, School of Engineering. Senior Member AIAA.
‡Professor, School of Aerospace, Civil and Mechanical Engineering.
§Senior Lecturer, Division of Physics, School of Physical Sciences.

Introduction

THERE are very few experimental studies on the flow over a flat plate at near suborbital or at superorbital flow speeds. The flows over flat plates generated in the X2 expansion tube are among the highest total-enthalpy flows ever reported in literature, with only the flat-plate data of Neely [1] being at a higher total enthalpy. The flat-plate models used in the present investigation are larger than that used by Neely. The present models also have heat-flux gauges, allowing a greater insight into the physical mechanisms influencing the heat-flux distribution along the plate. The current investigation thus represents the most detailed high-enthalpy, flat-plate, heat-flux experiments ever conducted in an expansion tube.

In this paper, the reference-temperature method is used to predict the heat-flux distribution along a flat plate. Previous experimental investigations such as those by Mallinson et al. [2] and Neely [1] have shown that the reference-temperature method gives good

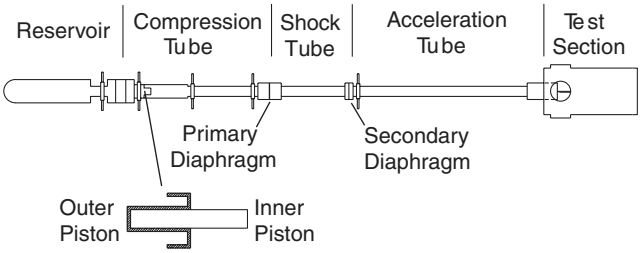

Fig. 1 A schematic of the X2 superorbital expansion tube.

agreement with experimental heat-flux distributions in high-enthalpy flows.

For the high-enthalpy flows generated in the X2 expansion tube, the heat fluxes are affected by the chemical state of the flow. The heat-flux predictions, modified by East el al. [3] to incorporate the effects of the flow chemistry, are compared with the experimental data.

Apparatus

X2 Superorbital Expansion

Tube X2 is a free-piston-driven superorbital expansion tube that uses an unsteady expansion process to increase the enthalpy of the flow [4]. A schematic of X2 is shown in Fig. 1. The X2 expansion tube is approximately 18-m long, with an exit diameter of 85 mm, and a usable test core of approximately 60-mm diameter. The compression tube incorporates an area change to accommodate a compound piston that compresses the driver gas in two stages. Initial compression occurs in a tube of 273-mm diameter using a 11.6-kg aluminum outer piston with a 25.1-kg inner piston mounted in the center of it. The inner piston extends 140 mm out of the front of the outer piston when it is mounted in the center of this piston. At the area change, the outer piston is stopped, allowing the inner piston to detach and further compress the driver gas in a tube of 91-mm diameter.

The launch station of X2 consists of a double-diaphragm arrangement that separates the high-pressure air in the reservoir from the compound piston before launch. After these diaphragms have ruptured, the high-pressure reservoir gas propels the compound piston down the compression tube. The compressed driver gas (normally helium or a mixture of argon and helium) causes the primary diaphragm to rupture, sending a shock wave through the test gas in the shock tube. The primary diaphragm used in X2 is either a 1.6- or 2-mm cold-rolled mild steel sheet. The corresponding rupturing pressures are 26 and 32 MPa, respectively. A light secondary diaphragm is used to separate the shock tube from the acceleration tube. For the current experiments, this secondary diaphragm consisted of a single sheet of cellophane 0.021-mm thick or, in the situation in which flow visualization was used, a single sheet of 0.015-mm-thick plastic. The plastic was required for the shots with resonantly enhanced interferometry, because the cellophane dissolved when exposed to the seeding solution used for the flow-visualization tests.

The secondary diaphragm is disintegrated by the passing of the shock wave generated by the rupture of the primary diaphragm [4]. The shock-heated test gas then undergoes an unsteady expansion down the acceleration tube before passing over the test model mounted at the downstream end of the acceleration tube. The theory and operation of X2 are detailed in Morgan [5]. The test flow conditions are altered by using different combinations of filling pressures and gases in the reservoir, compression tube, shock tube, and acceleration tube. The primary diaphragm thickness can also be varied. The primary diaphragms used and filling pressures and gases for the present tests are listed in Table 1.

Table 1 Filling pressures and primary diaphragm thicknesses for the nominal X2 flow conditions

Condition	Suborbital	Superorbital
Reservoir, MPa air	1.6	1.6
Compression tube, kPa He	53.6	53.6
Shock tube, kPa air	7.5	2.4
Acceleration tube, Pa air	30.0	1.0
Primary diaphragm, mm	1.6	1.6

Model and Instrumentation

The model consisted of a flat plate, 150-mm wide and 150-mm long. The width of the plate was larger than the diameter of the core flow of the expansion tube. Comparison between heat-flux measurements on plates of different widths indicated that having a plate wider than the core flow did not influence the heat flux down the center of the plate. The underside of the flat plate was beveled to give a leading-edge angle of 25 deg. The plate was attached to a base that was used to mount the model in the test section and provide aerodynamic shielding of the leads to the gauges from the test flow.

The model was equipped with flush-mounted nickel thin-film heat-flux gauges, located in staggered positions within 5 mm of the centerline of the plate. The gauges were manufactured in-house and consisted of a nickel film, 1-mm long $\times$ 0.3-mm wide$\times$ 0.3-μm thick, deposited onto fused quartz cylinders of 2.1-mm diameter. Nickel was used as the thin-film material due to its ability to be vacuum-deposited. This results in very thin films and gauges with short response times. A protective layer of silicone dioxide (SiO_2) was applied to the gauge surface to protect the thin films from erosion and the effects of ionization. Enameled wire leads were soldered to each gauge and the gauges were aged by baking them at 160°C for a minimum of 12 h to minimize possible hysteresis. The gauges and associated instrumentation have typical response times of 2 μs [6].

The gauges were mounted flush with the model surface. They were electrically isolated from the model and held in place by filling around the sides of the gauges with cyanoacrylate adhesive. Further details of the design, construction, and mounting of the thin-film gauges can be found in Hayne [7]. The heat-flux gauges were calibrated using a purpose-built computer-controlled calibration oven. Each thin-film gauge was calibrated using a predetermined calibration routine that heated and cooled the gauges between the temperatures of 35 and 100°C. The variation of gauge resistance with temperature was recorded and the slope of the resulting curve $\mathrm{d}R_G/\mathrm{d}T$ was calculated to give a calibration constant for each gauge. The calibration constant recorded for each gauge was divided by the gauge resistance to obtain the sensitivity value α_R required for the data processing to obtain the heat fluxes.

Wherever possible, the gauges were calibrated before they were mounted in the models, then again after mounting in the models before experiments were conducted, and for a third time, after the experiments were completed.

Data Acquisition

The X2 data were digitized and recorded at 0.25-μs intervals using multiple 21-channel transient data recorders, allowing 2 ms of data to be recorded for each test shot. The heat-flux-gauge signals were subsequently processed to obtain the heat-flux levels using the techniques detailed in Shultz and Jones [8].

Flow Conditions

The experiments were conducted at suborbital and superorbital flow conditions, with air as the test gas and acceleration gas. The nominal flow conditions are listed in Table 2. The flow conditions were calculated using a nonequilibrium computational simulation based on the code L1d [9]. The test gas was treated as a mixture of 77% nitrogen and 23% oxygen, with a five-species reaction model being adopted. The simulation was able to capture and model nonlinear effects such as attenuation of the shock speed in the acceleration tube.

The test flow consisted of several components, as seen in Fig. 2 for the suborbital condition. The starting shock that exits the acceleration

Table 2 X2 flow conditions

Flow parameter	Suborbital condition	Superorbital condition
h_0, MJ/kg	26.0	53.4
p_∞, kPa	12.0	1.5
T_∞, K	1800	1500
M_∞	6.9	10.5
Shock speed, m/s	6780	9600
a_∞, m/s	978	914
c_p, J/kg · K	1310	1245
γ	1.34	1.42
s/R_0	1.24	1.37
C_{N_2}	0.77	0.66
C_N	0.00	0.12
C_{O_2}	0.05	0.00
C_O	0.16	0.22
C_{NO}	0.02	0.00

tube is followed by a slug of the compressed acceleration gas. This compressed acceleration gas has a low density and high temperature compared with the test gas. The test gas exhausts through the end of the acceleration tube after the acceleration gas. The flow speed in the test section was taken to be equal to the speed of the shock at the exit of the acceleration tube. The steady test flow is terminated by the arrival of the expansion waves. Figure 2 shows typical pitot pressure and heat-flux traces showing features that can be associated with the different slugs of gas. The time taken for the acceleration gas to exhaust was estimated to be approximately 14 μs for the suborbital condition and 2 μs for the superorbital condition.

Flat-Plate Heat Flux

The Reynolds numbers, based on freestream conditions and plate length, were 3.0×10^5 and 9.8×10^4 for the suborbital and superorbital conditions, respectively. These values are low enough to ensure that the flow remained laminar along the entire length of the plate.

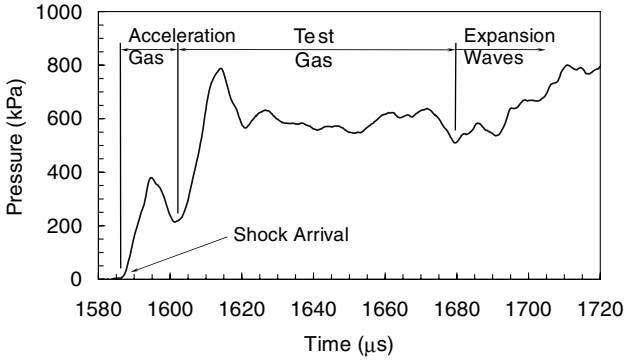

a)

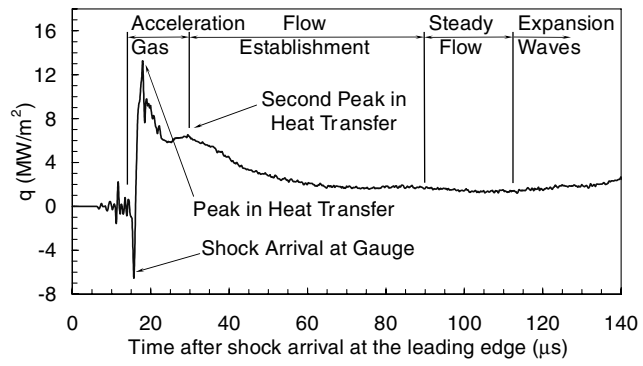

b)

Fig. 2 Suborbital condition measurements showing the major flow features: a) pitot pressure trace (shot 506) and b) Heat-flux trace (shot 454).

Reference-Temperature Method

In classical boundary-layer theory, the local skin friction for incompressible laminar flow over a flat plate is given by [10]

$$C_f = \frac{0.664}{\sqrt{Re_x}} \tag{1}$$

and the heat flux is given by

$$St = \frac{0.332}{\sqrt{Re_x}} Pr^{-\frac{2}{3}} \tag{2}$$

For compressible boundary layers, the reference-temperature or reference-enthalpy method is used to predict the skin friction and heat flux. The reference-temperature method is based on solutions to the compressible boundary-layer equations, as demonstrated by Dorrance [11]. The properties used in Eqs. (1) and (2) are evaluated at an intermediate reference temperature. The Young–Janssen reference temperature is

$$\frac{T^*}{T_e} = 1.28 + 0.023M_e^2 + 0.58\left(\frac{T_w}{T_e} - 1\right) \tag{3}$$

For a compressible laminar boundary layer on a flat plate, the local skin friction coefficient is given by [12]

$$C_f = \frac{0.664}{\sqrt{Re_x^*}} \tag{4}$$

Using the Reynolds analogy, the Stanton number can be written as [3,13]

$$St = \frac{0.332}{\sqrt{Re_x}} \sqrt{C^*} (Pr^*)^{-\frac{2}{3}} \tag{5}$$

where C^* and Pr^* are evaluated at the reference temperature. The Stanton number is evaluated as

$$St = \frac{q_w}{\rho_e u_e (h_r - h_w)} \tag{6}$$

where the recovery enthalpy h_r is defined by

$$h_r = h_e + \frac{\sqrt{Pr^*}}{2} u_e^2 \tag{7}$$

For flows at high enthalpies, Ott and Anderson [14] introduced a correction factor F into the Young–Janssen formula to account for the effects of nonequilibrium chemistry. The Ott and Anderson reference temperature is defined as

$$\left(\frac{T^*}{T_e}\right)_F = F\left[1.28 + 0.023M_e^2 + 0.58\left(\frac{T_w}{T_e} - 1\right)\right] \tag{8}$$

where F is derived empirically from numerical simulation results and is given by

$$F = 7.494 M_e^{-0.067} (T_e + T_w)^{-0.281} \tag{9}$$

The coefficient 7.494 in Eq. (9) has units of temperature, in Kelvin, to make the correlation factor nondimensional.

Gas-Phase Damköhler Number

The flow simulation results indicated that the chemistry in the freestream of the X2 expansion tube can be treated as frozen. Most of the oxygen is dissociated at the suborbital condition, and all of the oxygen and a fraction of the nitrogen are dissociated at the superorbital condition (see Table 2). With a frozen, partially dissociated freestream, it is necessary to determine whether the flow

in the boundary layer remains frozen or undergoes some chemical reactions.

To indicate whether the boundary layer remains frozen, Chung [15] and East et al. [3] showed that the gas-phase Damköhler number is the appropriate parameter. The gas-phase Damköhler number is the ratio of the characteristic boundary-layer particle-diffusion time τ_d to the characteristic reaction time τ_r, defined by

$$\Omega_g = \frac{\tau_d}{\tau_r} = \frac{4x}{u_e}\frac{k_{R_0}}{T^{(\omega+2)}}\left(\frac{p_e}{R_0}\right)^2 \tag{10}$$

Here, $k_{R_0} = 2k_R T^{\omega}$, where the exponent of temperature $\omega = 1.5$, and $R_0 = 8.31\ \mathrm{J\,mol^{-1}\cdot K^{-1}}$. The values of $2k_R$ that can be used in Eq. (10) are listed in Chung [15]. If $\Omega_g \ll 1$, the boundary layer will have frozen chemistry, whereas if $\Omega_g \gg 1$, the boundary layer will have equilibrium chemistry. When $\Omega_g \approx 1$, the boundary layer is in chemical nonequilibrium. For both the suborbital and superorbital conditions, the calculations showed that $\Omega_g \ll 1$, indicating that the boundary layers are expected to have frozen chemistry.

Catalytic Effects on Heat Flux

Gai et al. [16] investigated the effects of surface catalycity on the heat fluxes measured in a shock tunnel. They tested flat plates manufactured from aluminum and copper in the T3 shock tunnel. Noncatalytic effects were also examined and compared with the catalytic results by coating part of the model with silicon dioxide, which has a very low catalycity. Gai et al. conducted their experiments at flow enthalpies ranging between 13.0 and 19.0 MJ/kg using both air and nitrogen as the test gases. They found that both the catalytic and noncatalytic surfaces behaved essentially the same, indicating negligible surface recombination.

The flow-stagnation enthalpies for the current tests in X2 are significantly higher than those reported in Gai et al. [16]. To determine whether catalytic effects influence the surface heat fluxes, the surface Damköhler number can be calculated. Chung [15] defines the surface Damköhler number as the ratio of the characteristic surface diffusion time τ_d to the characteristic surface reaction time τ_s, given by

$$\Omega_s = \frac{\tau_d}{\tau_s} = \frac{Sc(\rho_w k_w)\sqrt{x}}{\sqrt{\rho_e u_e \mu_w (C_w/2)}} \tag{11}$$

Note that this can also be interpreted as the ratio of characteristic surface reaction rate to characteristic surface diffusion rate. The wall reaction rate k_w was taken from Fig. 4 of Chung [15].

When $\Omega_s \to 0$, the characteristic surface reaction rate is much smaller than the characteristic surface diffusion rate, indicating that the flow is approaching frozen chemistry at the surface. With frozen chemistry, the boundary layer near the surface becomes chemically inert. In the other extreme in which $\Omega_s \to \infty$, the characteristic surface reaction rate is much larger than the characteristic surface diffusion rate, indicating that the flow is approaching equilibrium chemistry at the surface. When equilibrium chemistry is reached, a state of local chemical equilibrium will exist, influencing the measured heat flux. When $\Omega_s \approx 1$, the characteristic surface reaction rate is approximately equal to the characteristic surface diffusion rate, indicating that recombination effects could start to influence the measured surface heat fluxes.

The value of k_w is influenced by the material constituting the surface of the model. The heat-flux gauges mounted in the model have a layer of silicone dioxide on their faces. SiO_2 has a value of γ_w of the order 10^{-4}, indicating that it is highly noncatalytic [3]. If the protective layer of silicone dioxide is incomplete or worn away due to ablation from the test flow, the nickel thin-film gauge is exposed and catalysis may proceed. The catalytic efficiencies and wall reaction rates for nickel and steel are presented in Chung [15].

Using the surface reaction rates from Chung [15] and the calculated flow conditions, the surface Damköhler number distributions calculated for both flow conditions indicate that it is likely that recombination of the oxygen occurs at the suborbital condition and that recombination of the oxygen and nitrogen is likely at the superorbital condition.

Effects of Chemistry on Heat Flux

The flat-plate heat-flux distributions can be calculated for both frozen and equilibrium chemistry. In the equilibrium limit, the Stanton number can be expressed as shown in Eqs. (5–7) [3]. For equilibrium-chemistry conditions, the recovery enthalpy h_r is given by [3]

$$(h_r)_{\mathrm{eq}} = c_{pf}T_e + h_{\mathrm{chem}} + h_{\mathrm{vib}} + \frac{\sqrt{Pr^*}}{2}u_e^2 \tag{12}$$

whereas for frozen-chemistry conditions, h_r is given by

$$(h_r)_f = c_{pf}T_e + \frac{\sqrt{Pr^*}}{2}u_e^2 \tag{13}$$

c_{pf} is the frozen specific heat at constant pressure.

The surface heat flux is dependent on the recombination of the atomic species, whether by gas-phase reactions within the boundary layer or by surface reactions in which the catalytic effect of the surface plays a dominant role when the gas-phase reactions are frozen. The analyses in the previous sections have shown that although the gas-phase Damköhler number indicates frozen chemistry in the boundary layer, the surface reaction Damköhler number suggests that nonequilibrium chemistry may be present.

The lowest heat-flux levels will occur when both the gas-phase and surface reactions are frozen. The magnitude of the fractional reduction from the equilibrium heat-flux levels is equal to $h_{\mathrm{chem}}/h_r - h_w$, where h_{chem} represents the chemical enthalpy that would result from the recombination of all of the atomic species present at the boundary-layer edge [3].

For a frozen boundary layer with a noncatalytic surface, the Stanton number can be expressed as [3]

$$St_f = St\left[1 - \left(\frac{h_{\mathrm{chem}}}{h_r - h_w}\right)\right] \tag{14}$$

where h_{chem} is the chemical potential enthalpy of the dissociated species, h_r is defined by Eq. (7), St is defined by Eq. (5), and h_{chem} is defined by

$$h_{\mathrm{chem}} = \sum_i C_i h_i^0 \tag{15}$$

where h_i^0 is the enthalpy of formation of species i.

If there is complete recombination, either through gas-phase reactions within the boundary layer or through a fully catalytic surface, it can be seen that $h_{\mathrm{chem}} = 0$ and the equilibrium value of heat flux is recovered. The values of h_{chem} for the suborbital and superorbital X2 conditions are shown in Table 3. Also included for comparison are the values of h_{chem} from the investigations of Mallinson [17] and Neely [1].

Experimental Results

Figure 3 shows the flat-plate heat-flux data obtained from three shots at the suborbital flow condition. It can be seen that the repeatability at this flow condition was good between shots.

Table 3 Values of h_{chem} and $1 - (h_{\mathrm{chem}}/h_r - h_w)$ for current experiments and those of Mallinson [17] and Neely [1]

Condition	h_0, MJ/kg	h_{chem}, MJ/kg	$1 - (h_{\mathrm{chem}}/h_r - h_w)$
Neely	108.0	13.30	0.83
X2 superorbital	53.4	6.55	0.84
X2 suborbital	26.0	2.60	0.88
Mallinson B	19.0	2.55	0.81
Mallinson D	13.8	1.40	0.86
Mallinson G	2.6	0.00	1.00

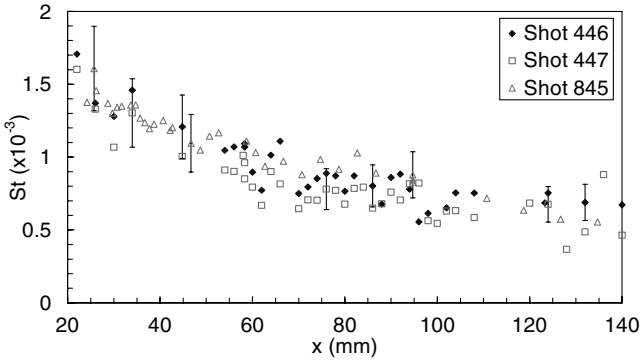

Fig. 3 Experimental heat-flux results for a flat plate at the suborbital flow condition.

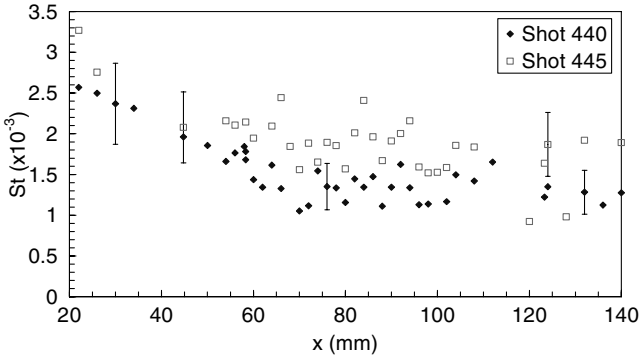

Fig. 4 Experimental heat-flux results for a flat plate at the superorbital flow condition.

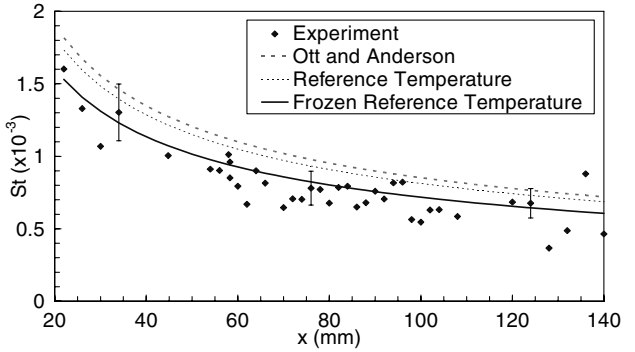

Fig. 5 Experimental and predicted flat-plate Stanton number distributions for shot 447 at the suborbital flow condition. The Ott and Anderson [14] prediction is given by using Eq. (9), the equilibrium reference-temperature prediction by Eq. (5) and the frozen reference-temperature prediction by Eq. (14).

Figure 4 shows the flat-plate heat-flux data obtained for two shots at the superorbital flow condition. The repeatability at this condition was not as good as the repeatability for the suborbital flow condition. This was due to the greater uncertainty in the acceleration-tube filling pressure at the superorbital condition compared with the suborbital condition.

Figure 5 shows the heat-flux data measured along the flat plate at the suborbital condition compared with the Stanton number distributions calculated using the equilibrium-chemistry reference-temperature method [Eq. (5)], the frozen-chemistry reference-temperature method [Eq. (14)], and the Ott and Anderson [14] modification given by Eq. (9). The Ott and Anderson modification is seen to overpredict the measured heat flux.

The equilibrium-chemistry reference-temperature method slightly overpredicts the heat flux. However, when the portion of chemical enthalpy contained in the frozen flow is included, as in the frozen-chemistry reference-temperature method, the heat-flux prediction lowers and agrees well with the data. The percentage difference between the equilibrium and frozen-chemistry heat-flux predictions is 12 and 16%, respectively, at the suborbital and superorbital conditions. The results indicate that the nonequilibrium surface chemistry causes minimal reduction of chemical enthalpy at the wall, suggesting that the chemistry is close to being frozen.

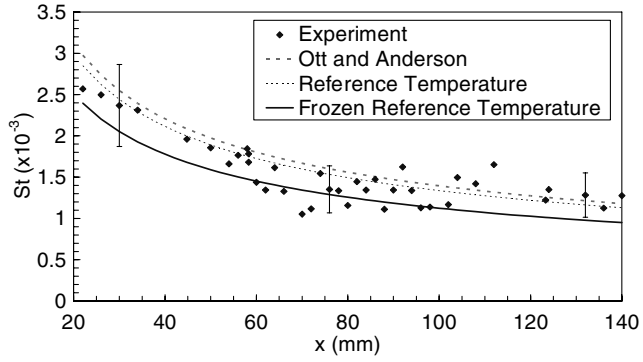

Fig. 6 Experimental and predicted flat-plate Stanton number distributions for shot 440 at the superorbital flow condition. The Ott and Anderson [14] prediction is given by using Eq. (9), the equilibrium reference-temperature prediction by Eq. (5) and the frozen reference-temperature prediction by Eq. (14).

The measured and calculated flat-plate heat-flux results at the superorbital condition are shown in Fig. 6. The overall Stanton number level is higher than for the suborbital results, with the predicted heat-flux levels calculated using the various methods showing the same trends as for the suborbital results. The agreement between the reference-temperature method modified for a frozen boundary layer and the data is very good, especially considering that Eq. (14) is based on the Blasius solution to the boundary-layer equations.

In Figs. 5 and 6, it can be seen that there is some scatter in the data. This is attributed to small imperfections in gauge mountings resulting in the gauges being slightly protruding or recessed. The heat-flux results also exhibit more scatter in the heat-flux levels further downstream on the plate. This is due to the smaller periods of established steady flow available in these locations. At distances further along the plate, the time required to scour the acceleration gas from the plate and establish steady flow increases. This time was shown to correlate well in terms of the distance from the leading edge of the plate [18]. At the superorbital condition, it is unlikely that steady flow is established after a distance of 100 mm from the leading edge. However, the steadiness evident in the heat-flux traces at these locations has led to the heat-flux levels being included for the gauges downstream of this point.

Figure 7 shows the current flat-plate heat-flux data compared with other high-enthalpy data from previous investigations. This figure is an extension of a figure previously presented by Mallinson [17]. The data are presented in terms of the variable

$$St = St' \frac{(Pr^*)^{\frac{2}{3}}}{\sqrt{C^*}[1 - (h_{\text{chem}}/h_r - h_w)]} \tag{16}$$

so that the data are clustered around the curve

$$St' = \frac{0.332}{\sqrt{Re_x}} \tag{17}$$

Most of the current experimental results lie within ±15% of Eq. (17). The outlying points are possibly due to flow unsteadiness toward the rear of the plate due to the shorter established test times. This conclusion is based on the fact that the outlying points all lie toward the rear of the plate (where the steady-flow period is minimal for flow over a flat plate). The data do, however, show that the trend observed by other experimenters is present in the current data. This indicates that the simple reference-enthalpy method, taking into

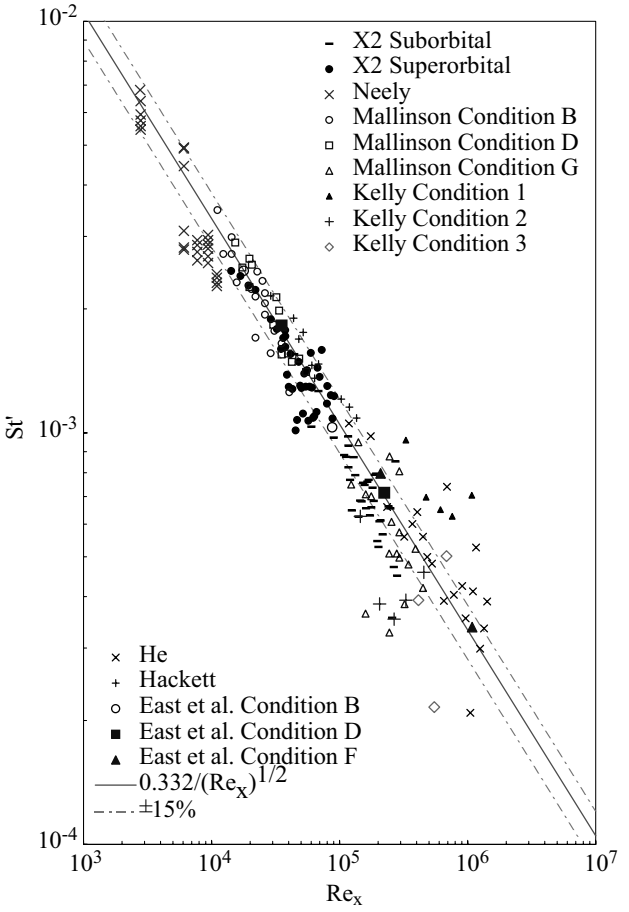

Fig. 7 Comparison of the current experimental results with other flat-plate heat-flux data in high-enthalpy flows. The data are sourced from Neely and Morgan [29], Mallinson et al. [2], Kelly [30], He [31], Hackett [32] and East et al. [3].

account the fractional reduction of heat flux due to frozen chemistry, works well at the present flow conditions. The results indicate that the X2 expansion tube test facility is capable of producing useful hypervelocity test flows.

Boundary-Layer Thickness

Prediction of the Boundary-Layer Thickness

To estimate the velocity-boundary-layer thickness for laminar flows, a number of expressions were derived based on compressibility transformations and the Crocco integral, given by

$$\frac{T}{T_e} = \frac{T_w}{T_e}(1-f') + f' + \sqrt{Pr}\frac{\gamma-1}{2}M_e^2(1-f')f' \tag{18}$$

White [10] derived an expression for δ_u by substituting Eq. (18) into the expression

$$\frac{\delta}{x}\sqrt{Re_x} = \sqrt{2}\int_0^{\eta_\delta}\frac{\rho_e}{\rho}\,\mathrm{d}\eta \tag{19}$$

given by Stewartson [19] and using the solution to the Blasius form of the boundary-layer equations in which $\eta(\delta_u) \approx 3.5$ to give

$$\delta_u \approx \frac{x}{\sqrt{Re_x}}\sqrt{C_w}\left[5.0 + \left(0.2 + 0.9\frac{T_w}{T_r}\right)(\gamma-1)M_e^2\right] \tag{20}$$

where T_r is defined by

$$T_r = T_e + \sqrt{Pr^*}\frac{\gamma-1}{2}M_e^2 \tag{21}$$

The accuracy of Eq. (20) in calculating the boundary-layer thickness was estimated by White [10] to be adequate across a range of Mach numbers and wall temperatures. An improved equation to estimate the boundary-layer thickness was derived by Mallinson et al. [2] by substituting the Crocco integral [Eq. (18)] into Eq. (19) to give

$$\frac{\delta}{x}\sqrt{Re_x} = 1.721\frac{T_w}{T_e} + 0.332\sqrt{Pr}(\gamma-1)M_e^2 + \sqrt{2}\int_0^{\eta_{\delta_T}} f'\,\mathrm{d}\eta \tag{22}$$

To evaluate

$$\int_0^{\eta_{\delta_T}} f'\,\mathrm{d}\eta$$

Mallinson et al. [2] used the solution to the Blasius form of the boundary-layer equations, integrated to $\eta_{\delta_T} \approx 4.125$ to account for a Prandtl number of 0.72. Evaluating the integral [2], Eq. (22) becomes¶

$$\delta_u = \frac{1.721x}{\sqrt{Re_x}}\left[2.397 + \frac{T_w}{T_e} + 0.193\sqrt{Pr}(\gamma-1)M_e^2\right] \tag{23}$$

Davis [20] derived an expression for the boundary-layer thickness for a frozen boundary layer. Like White [10] and Mallinson et al. [2], Davis used the Crocco integral, which he substituted into the inverted compressibility transformation:

$$\delta = \frac{\sqrt{2\xi}}{\rho_e u_e}\int_0^{\eta_e}\frac{\rho_e}{\rho}\,\mathrm{d}\eta = x\sqrt{\frac{2C}{Re_x}\frac{\mathrm{d}\,\ell n\,\xi}{\mathrm{d}\,\ell n\,x}}\int_0^{\eta_e}\frac{T}{T_e}\,\mathrm{d}\eta \tag{24}$$

For a flat-plate flow, $\mathrm{d}\,\ell n\,\xi/\mathrm{d}\,\ell n\,x = 1$, whereas C can be replaced by C^* to approximately account for cold walls by evaluating at the reference temperature. Taking the upper integration limit to be $f'(\eta_{99}) = 0.99$ and using the Blasius solution to the boundary-layer equations, Davis [20] obtained

$$\delta_u \approx 1.719x\sqrt{\frac{C^*}{Re_x}}\left[1.866 + \frac{T_w}{T_e} + 0.192\sqrt{Pr}(\gamma-1)M_e^2\right] \tag{25}$$

The only differences between the expressions of Mallinson et al. [2] and Davis [20] are the substitution of C^* for C by Davis and the larger integration limit used by Mallinson et al. The use of a larger integration limit by Mallinson et al. is interesting because the value of

$$\int_0^{\eta} f'\,\mathrm{d}\eta$$

is very sensitive to the choice of h. Mallinson et al. [2] integrated the values of f' to the value of $\eta \approx 4.125$, whereas Davis only integrated to $\eta \approx 3.5$. These integrations resulted in values of

$$\int_0^{\eta} f'\,\mathrm{d}\eta$$

being approximately 2.917 and 2.268, respectively. However, Stewartson [19] assumes the edge of the boundary layer to be $f'(\eta_{999}) = 0.999$, which makes

$$\int_0^{\eta} f'\,\mathrm{d}\eta \approx 3.050$$

The definition of the edge of the velocity boundary layer is thus very important in calculating the constants used in deriving expressions for the boundary-layer thickness based on the integration of the Crocco integral.

The inclusion of the Prandtl number in Eqs. (23) and (25) through the use of the Crocco integral in their derivations approximately accounts for a nonunity Prandtl number. For a nonequilibrium laminar hypersonic boundary layer in air, visualization and pitot pressure measurements made in the T3 shock tunnel by Baird et al.

¶The expression given in Mallinson et al. [2] contains an arithmetic error in the coefficient of the compressibility term.

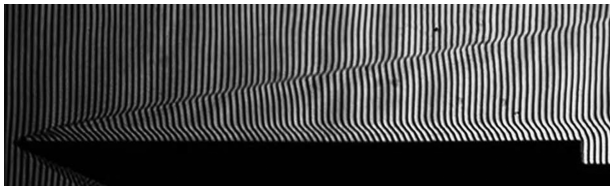

Fig. 8 Interferogram of the region upstream of the 2-mm step at the suborbital flow condition showing the fringe shifts associated with the thermal boundary layer.

[21] have suggested that the Prandtl number is greater than unity. A Prandtl number greater than one indicates that the velocity-boundary-layer thickness δ_u is greater than the thermal-boundary-layer thickness δ_T. Gai et al. [22] used the results of Baird et al. [21] to convert their measured thermal-boundary-layer thicknesses into the corresponding velocity-boundary-layer thicknesses. They then compared their results with predictions given by Eq. (20), which were found to overpredict the velocity-boundary-layer thickness at their moderate- and high-enthalpy conditions.

The use of a Prandtl number greater than unity by Gai et al. [22] is erroneous, because the $Pr > 1$ conclusion of Baird et al. [21] has subsequently being shown to be due to edge effects on the finite span model interfering with the interferograms [23]. Additionally, the theoretical work conducted by Hansen [24,25] has shown that the Prandtl number should vary between 0.5 and 1 for dissociated air. For the present investigation, it was assumed that the Prandtl number is given by the expression [26]

$$Pr = \frac{20\gamma}{39\gamma - 15} \tag{26}$$

Experimental Results

The flow visualization allowed the growth of the thermal boundary layer for a flat plate to be measured from the leading edge to a distance of 40 mm downstream of the leading edge [27]. Interferograms were obtained at both the suborbital and superorbital X2 conditions, as shown in Figs. 8 and 9, respectively. For scale, the distance from the leading edge to the step location is 48.4 mm. The fringe shifts in the interferograms are caused by variations in the density, which in turn is dependent on the temperature. Hence, the fringe shifts visible near the surface of the flat plates in the interferograms are a direct result of the thermal boundary layer. The direction of the fringe shifts is different in Figs. 8 and 9 due to how the background fringes are added to the image.

Figures 8 and 9 also show clearly that a merged layer, wherein the leading-edge shock wave and the developing boundary layer are "merged," exists in the vicinity of the leading edge for both sub- and superorbital flow conditions. The value of the rarefaction parameter in both cases is about 0.13, which is close to the rarefaction parameter criterion for a merged layer ($V = 0.15$).

For laminar flat-plate heat flux for a constant wall temperature, examination [28] of the nondimensionalized two-dimensional Navier-Stokes equations shows that the thickness of the velocity boundary layer, δ_u, varies with $Re^{-\frac{1}{2}}$. Similarly, examining the energy equation for steady laminar boundary-layer flow, it is found that the thermal-boundary-layer thickness δ_T is proportional to $Pe^{-\frac{1}{2}}$, where Pe is defined by the product $PrRe$. The ratio of the velocity- and thermal-boundary-layer thicknesses can thus be written as

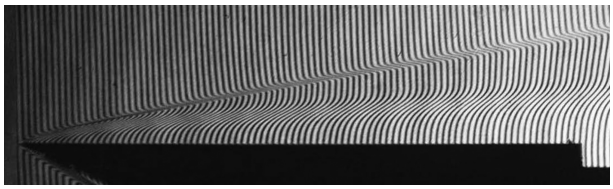

Fig. 9 Interferogram of the region upstream of the 2-mm step at the superorbital flow condition showing the fringe shifts associated with the thermal boundary layer.

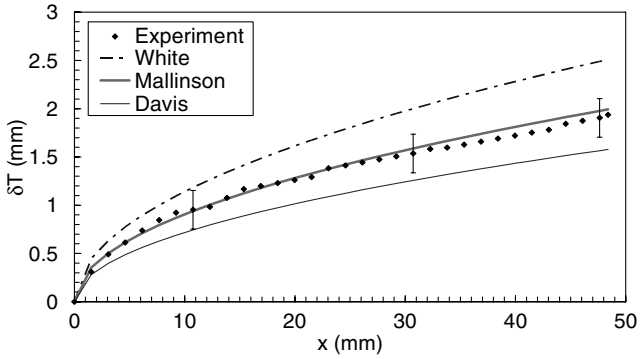

Fig. 10 The measured thermal-boundary-layer thickness at the suborbital condition compared with the predictions of White [10], Mallinson et al. [2], and Davis [20]. The data are from shot 496.

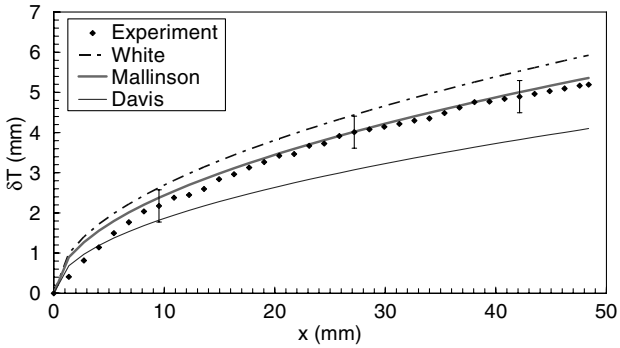

Fig. 11 The measured thermal-boundary-layer thickness at the superorbital condition compared with the predictions of White [10], Mallinson et al. [2], and Davis [20]. The data are from shot 498.

$$\frac{\delta_T}{\delta_u} \sim Pr^{-\frac{1}{2}} \tag{27}$$

The estimations of the thermal-boundary-layer thickness by Eqs. (20), (23), and (25) are compared with the measured thermal-boundary-layer thickness at the suborbital and superorbital conditions in Figs. 10 and 11. The calculated velocity-boundary-layer thicknesses were adjusted using Eq. (27) to their equivalent thermal-boundary-layer thicknesses. The edge of the thermal boundary layer was measured from the interferograms by identifying the location of the fringe shifts at the edge of the boundary layer. The errors in measurement of δ_T were estimated to be ± 0.2 and ± 0.4 mm at the suborbital and superorbital conditions, respectively.

The poor agreement with the White [10] formula is expected because it is empirically derived for perfect gas flows. The expression of Mallinson et al. [2] shows excellent agreement with the measured thermal-boundary-layer thickness, whereas the expression of Davis [20] underpredicts the boundary-layer thickness. The poor agreement with the Davis expression is due to his choice of integration limit across the boundary layer. If his integration limit was increased to the point at which the edge of the boundary layer is defined by $f'(\eta_{999}) = 0.999$, the agreement improves. However, the most common convention of defining the edge of the boundary layer is $f'(\eta_{99}) = 0.99$, indicating that the Mallinson et al. [2] expression is the preferred equation because it is consistent with the most widely practiced theory.

Conclusions

The flat-plate heat-flux data were shown to conform to the predicted heat-flux distributions based on the reference-enthalpy method corrected for frozen chemistry. Based on the work of East et al. [3], the analysis also showed that the influence of real gas effects, such as recombination and surface catalycity, were minimal for the present flow conditions. Existing theories were shown to be

adequate in predicting the measured heat fluxes at the enthalpies achieved in this investigation.

Interferograms were obtained in X2 using resonance enhancement of the fringe shift. This was the first time that this technique was used in an expansion tube to visualize flat-plate and rearward-facing step flows. Flow visualization allowed the thermal-boundary-layer thickness to be measured from the interferograms at the X2 flow conditions. The expression of Mallinson et al. [2] for the boundary-layer thickness was found to give very good agreement with the measured boundary-layer thickness.

Acknowledgments

The work described here was part of a project supported by the Australian Research Council (ARC) and the authors would like to express their sincere thanks to the ARC.

References

[1] Neely, A. J., "Experimental and Analytical Study of a Pilot Superorbital Expansion Tube for Aerothermodynamic Testing to 13 km/s in Air," Ph.D. Thesis, Department of Mechanical Engineering, Univ. of Queensland, Brisbane, Australia, 1996.

[2] Mallinson, S. G., Gai, S. L., and Mudford, N. R., "The Boundary Layer on a Flat Plate in Hypervelocity Flow," *The Aeronautical Journal*, Vol. 100, No. 994, Apr. 1996, pp. 135–141.

[3] East, R. A., Stalker, R. J., and Baird, J. P., "Measurements of Heat Transfer to a Flat Plate in a Dissociated High-Enthalpy Laminar Air Flow," *Journal of Fluid Mechanics*, Vol. 97, Apr. 1980, pp. 673–699.

[4] Doolan, C. J., "A Two-Stage Free Piston Driver for Hypervelocity Expansion Tubes," Ph.D. Thesis, Department of Mechanical Engineering, Univ. of Queensland, Brisbane, Australia, 1996.

[5] Morgan, R. G., "Free-Piston Driven Expansion Tubes," *Handbook of Shock Waves*, Vol. 1, Theoretical, Experimental and Numerical Techniques, Academic Press, New York, 2001, pp. 603–620.

[6] Palmer, R. A., "Measurement of Heat Transfer in Superorbital Flows," Ph.D. Thesis, Department of Mechanical Engineering, Univ. of Queensland, Brisbane, Australia, 1999.

[7] Hayne, M. J., "Method for the Construction of Thin-Film Heat Transfer Gauges," Div. of Mechanical Engineering, Univ. of Queensland, Rept. 20/2003, Brisbane, Australia, 2003.

[8] Shultz, D. L., and Jones, T. V., "Heat-Transfer Measurements in Short-Duration Hypersonic Facilities," AGARDograph 165, 1973.

[9] Jacobs, P. A., "Quasi-One-Dimensional Modeling of a Free-Piston Shock Tunnel," *AIAA Journal*, Vol. 32, No. 1, 1994, pp. 137–145.

[10] White, F. M., *Viscous Fluid flow*, 2nd ed., McGraw–Hill, New York, 1991.

[11] Dorrance, W. H., *Viscous Hypersonic Flow*, McGraw–Hill, New York, 1962.

[12] Anderson, J. D., *Hypersonics and High Temperature Gas Dynamics*, McGraw–Hill, New York, 1989.

[13] Mallinson, S. G., Gai, S. L., and Mudford, N. R., "The Interaction of a Shock Wave with a Laminar Boundary Layer at a Compression Corner in High-Enthalpy Flows Including Real Gas Effects," *Journal of Fluid Mechanics*, Vol. 342, July 1997, pp. 1–35.

[14] Ott, J. D., and Anderson, J. D., "Effects of Nonequilibrium Chemistry on the Reference Temperature Method and Reynolds Analogy," *Journal of Thermophysics and Heat Transfer*, Vol. 8, No. 2, 1994, pp. 381–384.

[15] Chung, P. M., "Chemically Reacting Nonequilibrium Boundary Layers," *Advances in Heat Transfer*, Vol. 2, June 1965, pp. 109–270.

[16] Gai, S. L., Mudford, N. R., Roberts, G. T., and Mallinson, S. G., "Effects of Catalycity and Boundary Layer Reactions on Surface Heat Flux in Hypersonic High Enthalpy Flows," *Shock Waves: Proceedings of the 20th International Symposium on Shock Waves*, edited by Sturtevant, B., Shepard, J., and Hornung, H., Vol. 1, World Scientific, Singapore, Republic of Singapore, 1995, pp. 317–322.

[17] Mallinson, S. G., "Shock Wave/Boundary Layer Interaction at a Compression Corner in Hypervelocity Flows," Ph.D. Thesis, Department of Aerospace and Mechanical Engineering, Australian Defence Force Academy, Univ. of New South Wales, Sydney, Australia, 1994.

[18] Hayne, M. J., Mee, D. J., Gai, S. L., Stewart, B., and Morgan, R. G., "Flow Establishment over Rearward-Facing Steps in High Enthalpy Flows," *Shock Waves: Proceedings of the 24th International Symposium on Shock Waves*, edited by Jiang, Z., Tsinghua Univ. Press, Beijing, and Springer, New York, 2004.

[19] Stewartson, K., *The Theory of Laminar Boundary Layers in Compressible Fluids*, Oxford Univ. Press, Oxford, 1964.

[20] Davis, J. P., "High-Enthalpy Shock/Boundary-Layer Interaction on a Double Wedge," Ph.D. Thesis, California Inst. of Technology, Pasadena, CA, 1999.

[21] Baird, J. P., Lyons, P., and Gai, S. L., "Measurements of Density and Velocity Profiles in Non-Equilibrium Laminar Hypersonic Boundary Layers in Air," *Shock Tubes and Waves: Proceedings of the 14th International Symposium on Shock Tubes and Shock Waves*, edited by Archer, R., and Milton, B., Sydney Shock Tube Symposium Publications, Kensington, NSW, Australia, 1983.

[22] Gai, S. L., Reynolds, N. T., Ross, C., and Baird, J. P., "Measurements of Heat Transfer in Separated High-Enthalpy Dissociated Laminar Hypersonic Flow Behind a Step," *Journal of Fluid Mechanics*, Vol. 199, pp. 541–561, Feb. 1989.

[23] O'Byrne, S., "Hypersonic Laminar Boundary Layers and Near-Wake Flows," Ph.D. Thesis, The Australian National Univ., Canberra, ACT, Australia, 2001.

[24] Hansen, C. F., "Note on the Prandtl Number for Dissociated Air," *Journal of the Aeronautical Sciences*, Vol. 20, No. 11, 1953, pp. 789–790.

[25] Hansen, C. F., "Approximations for the Thermodynamic and Transport Properties of High-Temperature Air," NACA TN 4150, 1958.

[26] Groth, C. P. T., Gottlieb, J. J., and Sullivan, P. A., "Numerical Investigation of High-Temperature Effects in the UTIAS-RPI Hypersonic Impulse Tunnel," *Canadian Journal of Physics*, Vol. 69, No. 7, 1991, pp. 897–918.

[27] McIntyre, T. J., Bishop, A. I., Eichmann, T. N., and Rubinsztein-Dunlop, H., "Enhanced Flow Visualization Using Near-Resonant Holographic Interferometry," *Applied Optics*, Vol. 42, No. 22, 2003, pp. 4445–4451.

[28] Pai, S.-I., *Viscous Flow Theory: I-Laminar Flow*, D. Van Nostrand Company Inc., Princeton, NJ, 1956.

[29] Neely, A. J., and Morgan, R. G., "The Superorbital Expansion Tube Concept, Experiment and Analysis," *The Aeronautical Journal*, Vol. 175, No. 973, Mar. 1994, pp. 97–105.

[30] Kelly, G., "A Study of Reynolds Analogy in a Hypersonic Boundary Layer Using a New Skin Friction Gauge," Ph.D. Thesis, Department of Mechanical Engineering, Univ. of Queensland, Brisbane, Australia, 1994.

[31] He, Y., "Boundary Layer Transition," Ph.D. Thesis, Department of Mechanical Engineering, Univ. of Queensland, Brisbane, Australia, 1992.

[32] Hackett, C. M., "Aerothermodynamic Heating Due to Shock Wave/Laminar Boundary Layer Interactions in High-Enthalpy Hypersonic Flow," AIAA Paper 93-3135, 1993.